Towards reconciling experimental and computational determinations of Earth's core thermal conductivity

Monica Pozzo [a,*], Christopher J. Davies [b], Dario Alfè [a,c]

[a] *Department of Earth Sciences, London Centre for Nanotechnology and Thomas Young Centre@UCL, University College London, Gower Street, London WC1E 6BT, United Kingdom*
[b] *School of Earth and Environment, University of Leeds, Leeds LS2 9JT, United Kingdom*
[c] *Dipartimento di Fisica Ettore Pancini, Università di Napoli Federico II, Monte S. Angelo, I-80126, Napoli, Italy*

A B S T R A C T

The thermal conductivity (κ) of Earth's core is a critical parameter that controls predictions of core cooling rate, inner core age and the power available to the geodynamo. However, the values of core thermal conductivity inferred from recent studies span a wide range due to the challenges of extrapolating to the pressure-temperature-composition (P-T-C) conditions of the core liquid. In particular, extrapolations of κ from direct experimental determinations are lower than ab initio calculations conducted at core conditions. We have performed density functional theory (DFT) calculations to determine the thermal conductivity and resistivity (ρ) of solid FeSi alloys with two compositions, 4 mol % and 15 mol % Si, at a range of temperatures (850-4350 K) and pressures (60-144 GPa) for ease of comparison with recent directly measured κ values. In agreement with recent experiments, our calculations show that for the larger Si composition the resistivity of the mixture increases substantially, compared to pure Fe, reaching its saturated value already at the lowest temperature investigated. As a result, the thermal conductivity of the mixture is also correspondingly reduced. We also analysed the effect of possible errors in the DFT calculations due to the neglect of electron-electron scattering (EES) processes. Our results show that experimental and EES-corrected DFT calculations of κ are actually consistent within uncertainties when compared directly at overlapping P-T-C conditions. We present new core thermal history models using our EES-corrected estimates of $\kappa = 75 - 81$ W m^{-1} K^{-1} at core-mantle boundary (CMB) conditions, which support previous determinations of late inner core formation around 400-700 Myrs ago and an early molten lower mantle.

1. Introduction

The Earth's core electrical ($\sigma = \rho^{-1}$) and thermal conductivities are two fundamental parameters for the modelling of the geodynamo and the thermal history of the Earth. The magnetic field is generated by electric currents in the outer core and the value of the electrical conductivity determines the entropy production that is required to sustain these currents against Ohmic dissipation. The currents are generated by convection, which is driven by thermal and/or compositional buoyancy. Thermal convection is possible if the rate of heat transfer by conduction is low enough, which would be the case for low enough thermal conductivity. Using a low assumed value of $\kappa = 28 - 46$ W m^{-1} K^{-1} (Stacey and Anderson, 2001; Stacey and Loper, 2007), core evolution models predict that

thermal convection driven by slow cooling provided ample power for magnetic field generation prior to inner core formation around 1 Gyr ago (Labrosse et al., 2001; Nimmo and Alfè, 2007). These models also favour thermally destabilising conditions throughout the core and hence the absence of a thermally stratified layer below the CMB.

New impetus was injected into the field around a decade ago, when a combination of new theoretical (Sha and Cohen, 2011; Pozzo et al., 2012; de Koker et al., 2012; Pozzo et al., 2013, 2014; Davies et al., 2015) and experimental studies (Gomi et al., 2013; Ohta et al., 2014, 2015; Gomi et al., 2016) suggested much higher thermal conductivity values of $100 - 240$ W m^{-1} K^{-1}, from CMB to inner-core-boundary (ICB) conditions. Gomi et al. (2013) were the first to point out the well known *saturation* mechanism for the reduced resistivity at high temperature, whereby this stops increasing when the scattering length reaches a value of the order of the atomic distances, the so called Mott-Ioffe-Regel limit

* Corresponding author.
  E-mail address: m.pozzo@ucl.ac.uk (M. Pozzo).

(Ioffe and Regel, 1960). This mechanism was also later supported by DFT calculations (Pozzo and Alfè, 2016a). Using these high κ values, core evolution models predicted striking differences from previous results. They showed that maintaining the dynamo for 3.5 Gyrs required much faster cooling rates, a young inner core of only 0.5 Gyrs, and early core temperatures far exceeding current estimates of the lower mantle solidus (Davies, 2015; Labrosse, 2015; Nimmo, 2015). Additionally, the higher κ values favour thermal stratification at the top of the core (Gomi et al., 2013; Davies et al., 2015).

Recently, Davies and Greenwood (in press) have estimated a range of $70 - 110$ W m^{-1} K^{-1} for κ for various Fe-O-Si mixtures at CMB conditions based on consistent extrapolation from a number of recent studies. A thorough review of ρ measurements and calculations of Fe and FeSi alloys at Earth's and other planetary cores conditions has also been recently published by Berrada and Secco (2021). They point out some discrepancies in the electrical resistivity values between theoretical and experimental studies, which may be ascribed to inconsistencies in measurements and modelling due to different techniques being used, together with a range of pressures and temperatures values attributed to planetary cores. They also find that values of Fe-alloys at Earth's CMB and ICB do not seem to significantly deviate from that of pure Fe.

The drastic changes to the standard model of core evolution implied by high thermal conductivity have driven numerous investigations, including analysis of the paleomagnetic record for signs of inner core formation (Biggin et al., 2015; Bono et al., 2019) and the proposal of new compositional buoyancy sources to alleviate the high cooling rates preceding inner core formation (O'Rourke and Stevenson, 2016; Badro et al., 2016; Hirose et al., 2017; Mittal et al., 2020). Numerous studies have also sought to determine thermal conductivity of iron alloys over a wide range of P-T-C conditions; however, this effort has led to divergent results. A key issue is whether the apparent disagreement reflects differences in 1) experimental vs computational approaches; 2) assumptions regarding extrapolation to core conditions.

Here we address this issue by calculating κ and ρ of iron alloys at P-T-C conditions used in recent experimental studies, which permits direct comparison between these two complementary approaches. This is crucial, since although theoretical and experimental findings agree with high values of σ for the Earth's core, such an agreement has not yet been reached for κ. In particular, Konôpková et al. (2016) inferred a low thermal conductivity value of 33 W m^{-1} K^{-1} at CMB conditions: this value was derived from a model that used direct measurements of κ at 112 GPa at various temperatures, and included resistivity data at room T extrapolated to 112 GPa and also shock wave resistivity data interpolated to 112 GPa, which were all converted to κ using the Wiedemann-Franz law $\kappa = \sigma L T$ (where T is the temperature) and a value of 1.9×10^{-8} W Ω K^{-2} for the Lorenz parameter L. This result was in stark disagreement with the value of $\kappa = 90$ W m^{-1} K^{-1} found by Ohta et al. (2016), from their ρ measurements, taking account of resistivity saturation and the Wiedemann-Franz law with an ideal value $L_0 = 2.44 \times 10^{-8}$ W Ω K^{-2}. To reconcile the two sets of measurements would require using in the Ohta et al. (2016) data a value of L to be one third of L_0, which is much lower than values obtained by direct calculation (de Koker et al., 2012; Pozzo et al., 2012, 2013, 2014; Pozzo and Alfè, 2016b; Secco, 2017; Pourovskii et al., 2020) and which would also need to have a strong pressure and temperature dependence. Indeed, Konôpková et al. (2016) noted that their minimum measured thermal conductivity did not include saturation (on the basis that resistivity saturation in Fe at extreme PT conditions was not clearly confirmed by theoretical studies and because available saturation models could not satisfactorily describe the data). However, they pointed out that if they assumed that resistivity saturation had occurred, then thermal conductivities at core conditions would be somewhat higher, 60-80 W m^{-1} K^{-1}, than obtained from their modelling.

More recently, Zhang et al. (2020) reported new measurements of σ and κ of hcp iron up to pressures of 180 GPa and temperatures of 4000 K. Their results fall somewhat in the middle between those of Konôpková et al. (2016) and Ohta et al. (2016). They also report values of the Lorenz parameter between 2.0 and 2.3 $\times 10^{-8}$ W Ω K^{-2}, which are somewhat lower than L_0 but show no dramatic pressure and/or temperature dependence. Additional recent experiments by Hsieh et al. (2020) were performed on pure iron at ambient temperature, and on Fe$_{0.96}$Si$_{0.04}$ and Fe$_{0.85}$Si$_{0.15}$ mixtures, both at ambient and at temperatures up to 3300 K. For pure iron at ambient temperature, κ values of up to 120 W m^{-1} K^{-1} were reported at pressures of 120 GPa, while for the mixtures the thermal conductivities were much reduced. At higher than ambient temperatures the thermal conductivities of the mixtures increased compared to the room temperature values, as expected, and it is expected that also those of pure iron would increase correspondingly, even though Hsieh et al. (2020) argue (without measuring them) that they would decrease, to the point of being in agreement with the low values of $\simeq 33$ W m^{-1} K^{-1} measured by Konôpková et al. (2016). For this to happen, the Lorenz number would have to show a strong decrease with temperature, because ρ increases at most linearly with temperature (and less than linearly once saturation starts to have an effect), which is incompatible with the values of the Lorenz parameter of 2.0-2.3 $\times 10^{-8}$ W Ω K^{-2} reported by Zhang et al. (2020). In fact, departure from L_0 has been noted for both pure iron and iron alloys in previous theoretical calculations (de Koker et al., 2012; Pozzo et al., 2012; Pozzo et al., 2013; Pozzo et al., 2014; Pozzo and Alfè, 2016b; Pourovskii et al., 2020). These show that the Wiedemann-Franz law strongly depends on temperature and alloy composition, providing Lorenz number values ranging from 1.6 to 2.8 $\times 10^{-8}$ W Ω K^{-2}, but these values are still far too large to reconcile the very low thermal conductivity values reported in Konôpková et al. (2016).

On the theoretical side, it has been pointed out that one possible problem with DFT calculations is the incomplete treatment of the electron-electron scattering (EES) mechanism. This was initially addressed by Pourovskii et al. (2017), who published new results obtained with post DFT methods based on dynamical mean field theory (DMFT) techniques. By taking into account both EES and electron-lattice scattering (ELS), they found $\kappa = 190$ W m^{-1} K^{-1} at Earth's inner core (IC) conditions and a Lorenz parameter $L = 2.04 \times 10^{-8}$ W Ω K^{-2}, which is lower than L_0, but still much higher than what would be required to reconcile the experimental value of ~ 50 W m^{-1} K^{-1} inferred from measurements by Konôpková et al. (2016) at IC conditions. A similar theoretical approach, also based on DMFT, was used by Xu et al. (2018), who obtained $\kappa = 150$ W m^{-1} K^{-1} at similar conditions. The DMFT based reported values of κ were substantially lower than the DFT value (about 240 W m^{-1} K^{-1}; Pozzo et al., 2014), suggesting a sizeable contribution of the EES mechanism, however, those calculations were performed on a perfect Fe crystal. Since EES depends on the value of the electron density of states at the Fermi energy, and since this is significantly affected by thermal disorder, it is expected that the contribution of EES to the thermal and electrical conductivities would also be significantly affected by thermal disorder, an effect which was not included in Pourovskii et al. (2017) and Xu et al. (2018), although the latter did report preliminary results for snapshots of a system representing the liquid and found that EES increases with thermal disorder. Hausoel et al. (2017) studied face-centred-cubic Ni at Earth's core conditions, and found that thermal disorder did not affect correlation much. The work of Zhang et al. (2020) mentioned above also included a theoretical study of ρ of hcp Fe. Calculations were performed either including only the ELS term, or both ELS and EES (ELS+EES), showing

that the two sets of results are close at low temperature, but deviate significantly from each other as temperature is increased. The calculations were again performed on the perfect hcp crystal, however, the authors also reported one ELS+EES calculation at T = 2000 K performed on snapshots of the solid including thermal disorder (ELS+EES+TS). At this temperature the difference between the ELS and the ELS+EES calculations is small, but the ELS+EES+TS results appear to be closer to the ELS one than to the ELS+EES, again suggesting that thermal disorder moderates the inclusion of EES substantially.

More recently, some of us have re-visited the electronic correlations and transport in pure iron at Earth's core conditions (Pourovskii et al., 2020) using DMFT. We studied both the hexagonal-closed-packed (hcp) and the body-centred-cubic (bcc) structures at 330 GPa and 5800 K, and found that the inclusion of EES lowers κ, but we also found that once thermal disorder is introduced this reduction is at most 24%, a much more moderate effect compared to the case in which calculations are performed on the perfect crystal. By contrast, ρ is much less affected by the inclusion of EES, increasing by only 9% over the ELS value.

Here we have extended our previous calculations on ρ of hcp Fe reported in Pozzo and Alfè (2016a, 2016b) by including κ values, and we have also performed calculations at similar pressure/temperature conditions on the two mixtures $Fe_{0.96}Si_{0.04}$ and $Fe_{0.85}Si_{0.15}$, which allow a more direct comparison with the most recent experiments of Hsieh et al. (2020) and Inoue et al. (2020). The calculations have been performed using DFT and the Kubo-Greenwood approach (Kubo, 1957; Greenwood, 1958) for ρ and the Chester-Thellung-Kubo-Greenwood approach (Chester and Thellung, 1961) for the electronic contribution to κ. The ionic contribution to κ is expected to be small and, as in previous studies, it has been neglected - it might increase the total thermal conductivity by only 2.5 to 4 $W\,m^{-1}\,K^{-1}$, depending on pressure/temperature conditions (Pozzo et al., 2012). Once the possible overestimation of κ due to the inclusion of only the ELS term is taken into account, we find that our results are compatible with the experimental measurements. Our calculations also confirm the remarkable reduction of thermal conductivity of the mixtures compared to that of pure iron, found in the experimental data (Hsieh et al., 2020), especially for the mixture with the larger amount of silicon.

2. Techniques

All the DFT calculations for this work were performed by using similar techniques to those used in our previous papers (Alfè et al., 2012; Pozzo et al., 2012, 2013, 2014; Pozzo and Alfè, 2016a, 2016b). The VASP code simulation package (Kresse and Furthmuller, 1996) was used with the projector augmented wave (PAW) method (Blöchl, 1994; Kresse and Joubert, 1999), together with the Perdew-Wang (Wang and Perdew, 1991) functional (PW91). We used PAW potentials with [Ne]$3s^2$ and [Ne] core for iron and silicon, and respective valence configurations $3p^64s^13d^7$ and $3s^23p^2$, with core radii of 1.16 Å and 0.79 Å. A plane-wave basis set was used to expand the electronic wave-functions with an energy cutoff of 380 eV. Electronic levels were occupied according to Fermi-Dirac statistics. Configurations in the canonical ensemble were generated by running molecular dynamics (MD) simulations, in which temperature was controlled by a combination of a Nosé (Nosé, 1984) and an Andersen (Andersen, 1980) thermostat, using a time step of 1 fs and using the Γ point only to sample the Brillouin zone. An efficient charge density extrapolation was used to speed up the MD simulations (Alfè, 1999), which we typically ran for 9-12 ps, discarded the first ps to allow for equilibration, and extracted typically 30-40 configurations equally spaced in time on which we computed the electrical and thermal conduc-

Table 1

Temperature (T), pressure (P), resistivity (ρ), thermal conductivity (κ) and Lorenz parameter (L) for pure solid iron from Pozzo and Alfè (2016a, 2016b).

T (K)	P (GPa)	ρ ($10^{-6}\,\Omega\,m$)	κ ($W\,m^{-1}\,K^{-1}$)	L ($10^{-8}\,W\,\Omega\,K^{-2}$)
4350	97	0.716(2)	171(1)	2.81
3350	85	0.653(3)	141(1)	2.75
2350	73	0.527(4)	114(1)	2.56
1850	68	0.424(3)	105(1)	2.41
1350	63	0.321(3)	99(1)	2.35
850	59	0.200(2)	100(1)	2.35

Table 2

Temperature (T), pressure (P), resistivity (ρ), thermal conductivity (κ) and Lorenz parameter (L) for $Fe_{0.96}Si_{0.04}$ solid (composition is given in mol %).

T (K)	P (GPa)	ρ ($10^{-6}\,\Omega\,m$)	κ ($W\,m^{-1}\,K^{-1}$)	L ($10^{-8}\,W\,\Omega\,K^{-2}$)
4350	99	0.766(2)	154.3(5)	2.72
3350	86	0.730(2)	125.7(3)	2.74
2350	75	0.660(2)	93.4(2)	2.62
2050	72	0.626(2)	84.5(3)	2.58
1850	70	0.605(2)	77.5(3)	2.53
1350	65	0.529(2)	62.3(2)	2.44
850	61	0.455(2)	44.2(1)	2.36

tivities, using 2 **k**-points to sample the Brillouin zone. The electrical conductivity was computed using the Kubo-Greenwood (Kubo, 1957; Greenwood, 1958) formula and the thermal conductivity using the Chester-Thellung-Kubo-Greenwood (Chester and Thellung, 1961) formula, as implemented in VASP by Desjarlais (Desjarlais et al., 2002). Lorenz parameters were obtained as $L = \kappa/\sigma T$.

The calculations were performed on supercells containing 490 atoms, with total of 20 and 74 Fe atoms randomly substituted with Si atoms to obtain 4 mol % and 15 mol % alloying compositions. For the 15 mol % alloying composition, we also checked convergence of the electrical and thermal conductivities with respect to the size of the simulation supercell for the lowest temperature of 850 K. This was done by performing additional calculations with two supercells including 768 and 972 atoms in which we substituted 115 and 146 Fe atoms with Si respectively. We also checked that in all our simulations the system under scrutiny remained solid throughout.

3. Results

In Table 1 we report ρ data of pure solid iron as computed earlier (Pozzo and Alfè, 2016a), also including κ data and the Lorenz parameter L (Pozzo and Alfè, 2016b). In Tables 2 and 3 we report ρ and κ data computed in this work for hcp iron with 4% and 15% Si respectively (where compositions are given in mol %).

The resistivity data for the three systems are also plotted in Fig. 1. We report our raw DFT data, as well as these data increased by 9%, which is the likely correction due to lack of the EES contribution missing in our calculations, as quantified in Pourovskii et al. (2020). Perhaps the most striking feature in Fig. 1 is the large increase in the resistivity of the 15% Si mixture compared with that of pure iron, and also compared with that of the system with 4% Si. Interestingly, the resistivity of the 15% Si mixture is also almost independent on temperature and rather shows a small negative temperature dependence. This trend was observed at much lower and constant pressures in the solid state of high silicon Fe-Si alloys by Baum et al. (1967) at 1 atm, and also in recent work by Berrada et al. (2020) on solid Fe8.5wt%Si and increasingly so on Fe17wt%Si at pressures in a 3-5 GPa range. It was also reported for solid and lower silicon Fe4.5wt%Si by Silber et al. (2019) at pressures in a 3-9 GPa range.

Table 3

Temperature (T), pressure (P), resistivity (ρ), thermal conductivity (κ) and Lorenz parameter (L) for $Fe_{0.85}Si_{0.15}$ solid (composition is given in mol %).

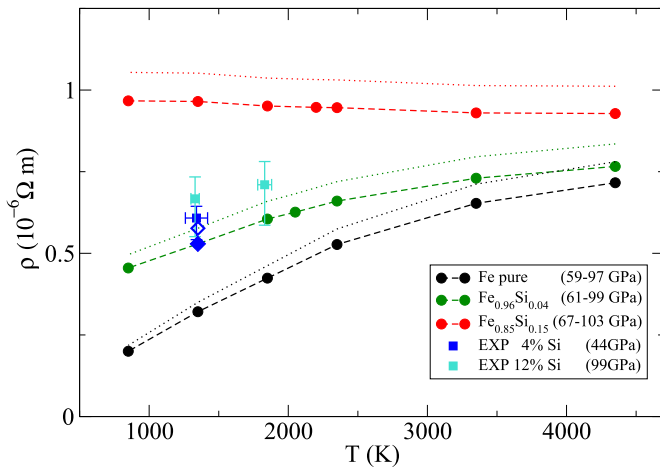| T (K)	P (GPa)	ρ ($10^{-6}\,\Omega\,m$)	κ ($W\,m^{-1}\,K^{-1}$)	L ($10^{-8}\,W\,\Omega\,K^{-2}$)
4350	103	0.928(2)	120.2(2)	2.56
3350	92	0.930(2)	95.0(2)	2.64
3000	144	0.883(2)	90.5(2)	2.66
3000	106	0.916(2)	87.1(2)	2.66
2500	106	0.917(2)	72.1(2)	2.65
2350	81	0.946(2)	65.5(1)	2.64
2200	79	0.947(2)	61.4(1)	2.64
1850	76	0.951(2)	50.0(1)	2.57
1350	72	0.965(2)	35.4(1)	2.53
850	67	0.967(2)	21.5(1)	2.45

Fig. 1. Electrical resistivity (ρ) of pure solid Fe, $Fe_{0.96}Si_{0.04}$ and $Fe_{0.85}Si_{0.15}$ as a function of temperature (T). Calculations have been performed at constant volumes and so pressures increase with temperature, as indicated in the legend for the respective cases. Also shown present calculations increased by 9% (dotted lines), which is an estimate of the possible error due to absence of EES contributions (see text). Experimental values for similar mixtures from Inoue et al. (2020) are also shown. The blue filled diamond is from present calculations at similar PT as used in experiments (44 GPa, 1340 K); the corresponding computed value increased by 9% is shown as an open diamond (see text for details). (For interpretation of the colours in the figures, the reader is referred to the web version of this article.)

As previously highlighted (Pozzo et al., 2011), large resistivities calculated within the Kubo-Greenwood approach may be an arte-fact of the size of the simulation cell, which must be large enough to accommodate the length of the mean free path. For instance, we found that in liquid Na at ambient conditions we needed to use simulation cells including at least 1000 atoms to obtain a converged resistivity. This potential problem is of course more likely to appear at low temperature, where the mean free paths are longer. For this reason, in addition to the simulation performed with a 490-atom cell, we repeated the calculation for the 15% Si mixture at 850 K using 768- and 972-atom cells. The electrical and thermal conductivities computed with these larger cells were indistinguishable from those obtained with the smaller 490-atom cells, indicating that the large resistivity found for this system is a real effect. The apparent temperature independence of this resistivity also indicates that the determination of the mean free path is dominated by the presence of the Si impurities rather than by temperature.

Experimental values for two similar Si composition mixtures (2 and 6.5 wt %, corresponding to 4 and 12 mol %) from Inoue et al. (2020) are also plotted in Fig. 1. The lower temperature experimental point for the 4% Si mixture (44 GPa, 1340 K) is in agreement with our corrected computed value (65 GPa, 1350 K),
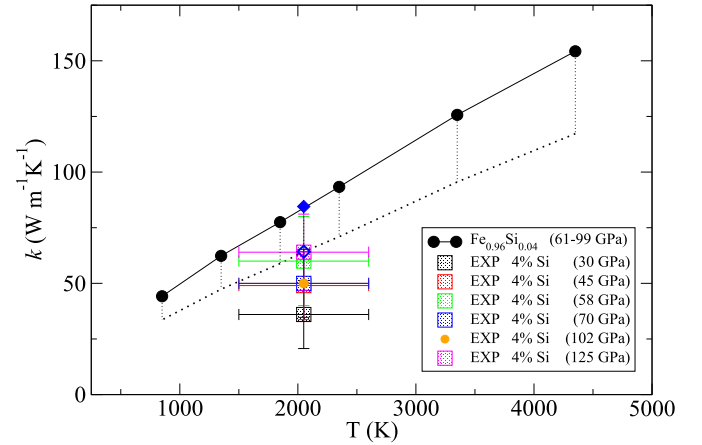

Fig. 2. Thermal conductivity of $Fe_{0.96}Si_{0.04}$ solid as a function of temperature. Present calculations (black filled circles) cover 61-99 GPa in the 850-4350 K temperature range (see Table 2). Also shown present calculations reduced by 24% (dotted line), which is an estimate of the possible error due to absence of EES contributions (see text). The experimental data for the same mixture from Hsieh et al. (2020) are plotted in different coloured symbols as shown in the inset legend. The blue filled diamond is from present calculations at the same PT experimental conditions (70 GPa, 2050 K); the corresponding computed value reduced by 24% is shown as an open diamond.
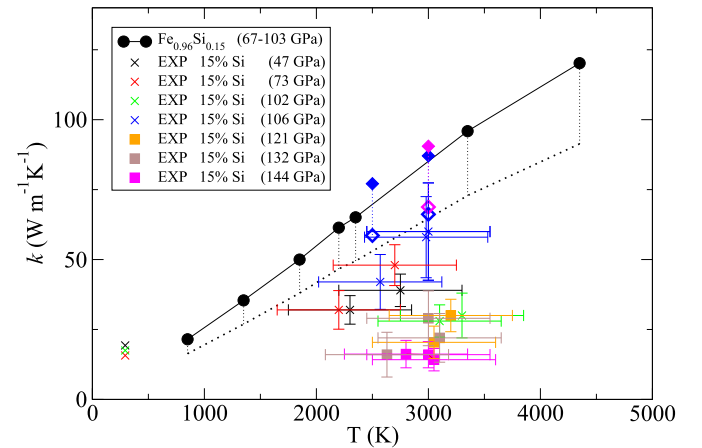

Fig. 3. Thermal conductivity of $Fe_{0.85}Si_{0.15}$ solid as a function of temperature. Present calculations (black filled circles) cover 67-103 GPa in the 850-4350 K temperature range (see Table 3). Also shown present calculations reduced by 24% (dotted line), which is an estimate of the possible error due to absence of EES contributions (see text). The experimental data for the same mixture from Hsieh et al. (2020) are plotted in different coloured symbols as shown in the inset legend. Filled diamonds are present calculations at the same PT experimental conditions, plotted with corresponding colours; computed values reduced by 24% are shown as open diamonds.

and the small difference in pressure between the two set of data is not expected to affect the value of the resistivity appreciably (Secco, private communication).

Thermal conductivities for the 4% and 15% Si mixtures are plotted in Figs. 2 and 3. We report our raw DFT data, as well as these data reduced by 24%, which is the likely correction due to lack of the EES contribution missing in our calculations. In both figures we also report the experimental data of Hsieh et al. (2020). They note that temperature values are average measurement temperatures. They do not provide an uncertainty value, but from the caption of their Supplementary Table 5 we can infer that it is likely to be of the order of 550 K. In the case of $Fe_{0.96}Si_{0.04}$, Hsieh et al. (2020) report values of κ at different pressures but at the same temperature of 2050 K. From Fig. 2 it is clear that our calculated κ at 2050 K and 72 GPa is higher than the corresponding experimental value

(2050 K and 70 GPa, blue square), but agreement is reached after taking into account the effect of EES contributions (see dotted line) plus the experimental measurement uncertainties.

Similarly, our calculated values for κ of the $Fe_{0.85}Si_{0.15}$ mixture are higher than experimental ones (Hsieh, 2020), as shown in Fig. 3. In this case the two sets of results could be still compatible for at least some of the data (e.g. 2500 and 3000 K at 106 GPa) once the possible EES effect (although as suggested by Zhang et al. (2020) this error should decrease with decreasing temperature) and the experimental measurements uncertainties are taken into account. We also note that the experimental data are quite scattered, indicating the likely size of the error. At high pressure (144 GPa and 3000 K) the experiments report very low thermal conductivity values, which are incompatible with our calculated ones. We note that κ experimental measured values increase for increasing temperature at every given pressure as predicted by our computational results until 106 GPa. At higher pressures, experimental values are not following the expected behaviour, since they do not increase for increasing temperature values, making us wonder if this could be due to the presence of (partial) melt in the experimental samples.

Another important aspect to consider is the onset of the saturation effect. As shown in Fig. 1, the onset of saturation behaviour for $Fe_{0.96}Si_{0.04}$ solid is clearly visible at temperatures above 2500 K. We previously noticed the same effect for pure solid Fe (Pozzo and Alfè, 2016a). This seems to be in contradiction with recent findings by Zhang et al. (2020) on the resistivity of solid Fe up to ~ 3000 K, who point to an apparent almost linear dependence on temperature. However, from our results (Pozzo and Alfè, 2016a) at the pressure values studied by Zhang et al. we would expect the onset of the saturation behaviour to start at about 3600 K, which is well above their maximum experimental working temperature. By contrast, Inoue et al. (2020), despite sampling temperatures up to 3120 K only, were able to detect the onset of the saturation behaviour for hcp Fe-2, 4 and 6.5 wt.% Si. From our $Fe_{0.96}Si_{0.04}$ solid results, we can see that in the case of a 4% mixture the onset of the saturation behaviour starts at a lower temperature of about 2500 K and it was indeed detected by Inoue et al. Therefore we argue that the resistivity saturation behaviour in Fe and iron alloys should be easily detected in experimental investigations, providing these sample a temperature range up to large enough values.

4. Geophysical implications

The results presented in Section 3 show that experimental and theoretical κ values are consistent within uncertainties when compared directly at overlapping P-T-C conditions. Previously, we calculated values of 107, 99 and 101 $W\,m^{-1}\,K^{-1}$ at the top of the outer core for Fe-O-Si mixtures along three different adiabatic profiles, at temperatures of 5700, 5500 and 5300 K respectively (Pozzo et al., 2013; Davies et al., 2015). Here we would like to revisit the errors on those values by taking into account a possible 24% correction due to EES contributions. Therefore, we propose to replace our previous values at CMB conditions with a range of values spanning from 107, 99 and 101 $W\,m^{-1}\,K^{-1}$ to 81, 75 and 77 $W\,m^{-1}\,K^{-1}$ respectively.

To investigate the implications of these new κ values for Earth's core we estimate its thermal history using the model described in Davies (2015). Briefly, we integrate the core energy and entropy balances backwards in time for 3.5 Gyrs. The energy balance determines the core cooling rate by relating the CMB heat flow Q_{cmb} to the power sources in the core. We do not consider precipitation of oxides (e.g. O'Rourke and Stevenson, 2016; Hirose et al., 2017) because the onset and rate of precipitation are currently poorly constrained (Davies and Greenwood, in press). Adding precipitation of MgO could increase the predicted inner core age by a factor of
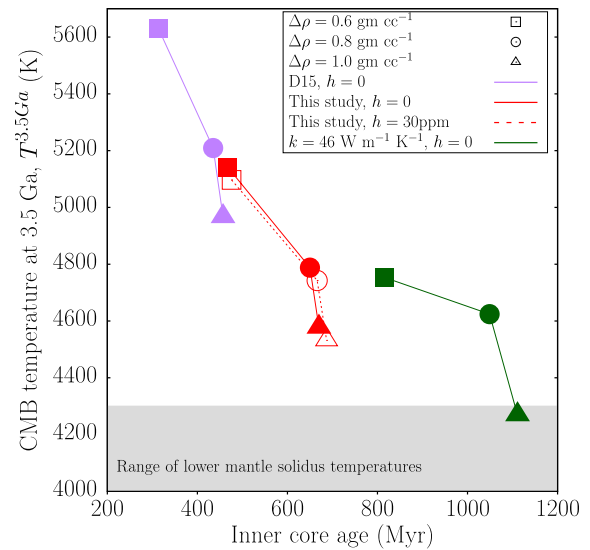

Fig. 4. Predicted inner core age and CMB temperature at 3.5 Gyrs ago from thermal history models for $\Delta\rho = 0.6, 0.8$ and 1.0 gm/cc and three sets of κ values: 46 $W\,m^{-1}\,K^{-1}$ (green symbols) as inferred by Stacey and Anderson (2001); our previous DFT-only κ values (purple) reported in Pozzo et al. (2013) and Davies et al. (2015); and our new proposed values from this study (red). Data from our current models also including 30 ppm ^{40}K are shown as red open symbols.

1.1-2 (Davies and Greenwood, in press). In addition, we omit terms due to compressional heating and heat of reaction since they are tiny compared to the leading terms (Gubbins et al., 2003; Davies, 2015; Nimmo, 2015). The final energy equation is then a balance between CMB heat flow and secular cooling, radiogenic heating, latent heat and gravitational energy release that accompany inner core growth. Dynamo activity is assessed using the entropy balance, which relates the entropy sources from secular cooling, radiogenic heating, latent heat and gravitational energy release to the entropy of thermal conduction (which depends on κ), and the dynamo entropy E_J that defines the entropy production due to dynamo action.

All parameter values except κ are taken from Davies et al. (2015). The main uncertainty in the calculation is the density jump $\Delta\rho$ at the ICB, which sets the core composition and melting temperature. We use the three values of $\Delta\rho = 0.6, 0.8$ and 1.0 gm/cc that span the uncertainties determined from normal mode studies (Masters and Gubbins, 2003) together with the corresponding compositions and temperature profiles in Davies et al. (2015). Following Nimmo (2015) we prescribe Q_{cmb} during the period of inner core growth and the entropy production E_J prior to inner core formation. This assumption generates a plausible variation of CMB heat flow with time. We vary the present Q_{cmb} value such that the model produces an E_J prior to inner core formation that is marginally positive, which is required to satisfy paleomagnetic predictions of continuous dynamo activity back to 3.5 Ga (Tarduno et al., 2010; Davies et al., 2022) and also yields a conservatively low core cooling rate and hence inner core age and ancient CMB temperature. All models are also required to match the present ICB radius of 1221 km.

Fig. 4 shows the predicted inner core age and CMB temperature at 3.5 Gyrs ago for the three values of $\Delta\rho$ and three sets of κ values: an old and low κ value of 46 $W\,m^{-1}\,K^{-1}$ (green symbols) inferred by Stacey and Anderson (2001); the DFT-only κ values (purple) reported in Pozzo et al. (2013) and Davies et al. (2015); and the new values (red). We also run models with the addition of 30 ppm ^{40}K as suggested by Xiong et al. (2018), which confirm that such a small amount of radiogenic heating has a negligible impact on the results. In all cases higher $\Delta\rho$ increases the inner core

age and decreases the ancient CMB temperature because enhanced gravitational power allows the dynamo to operate at lower cooling rate. As expected, the new results sit in-between the two older datasets, with a predicted inner core age of 400-700 Myrs. This range is broadly consistent with previous thermal history models that included high thermal conductivity (e.g. Driscoll and Bercovici, 2014; Labrosse, 2015; Davies et al., 2022). Maintaining the geodynamo with such a young inner core requires a rapid cooling rate over most of Earth's history, which implies that the core formed hot. All models predict that the ancient CMB temperature far exceeded estimates of the lower mantle solidus, suggesting an early molten lower mantle permitting efficient thermal and chemical exchange with the core (Davies et al., 2020).

Our calculations estimate the present-day adiabatic heat flow at the CMB to lie in the range 10-12 TW. Estimates of the total present CMB heat flow range from 7-17 TW (Nimmo, 2015) with recent work favouring Qcmb $\approx$15 TW (Frost et al., 2022). It is therefore possible that the top of the core is presently sub- or super-adiabatic, though the numbers above favour the former scenario. Nevertheless the sub-adiabatic case is of interest because independent geomagnetic (Buffett, 2012) and seismic (Helffrich and Kaneshima, 2010) observations have been used to infer the presence of a stratified layer atop the core. Sub-adiabatic conditions require the presence of a region below the CMB that is stable to thermal convection, though it may not be stable to convection overall since the destabilising chemical buoyancy arising from inner core growth renders the region susceptible to double-diffusive instabilities. Considering the minimum CMB heat flow of 7 TW, calculations with $k = 70$ W/m/K, similar to our values, estimated the maximum thickness of the thermally stable region to lie in the range 400-500 km (Davies and Greenwood, in press). The corresponding strength of thermal stratification is, however, too weak to match the model of Helffrich and Kaneshima (2010). This discussion suggests that any stratification in the upper core owes its existence to chemical (rather than thermal) effects, such as incomplete mixing during core formation (Landeau et al., 2017; Bouffard et al., 2020) or mass exchange with the mantle or basal magma ocean (Buffett and Seagle, 2010; Davies et al., 2020).

5. Conclusions

In this paper we have presented new DFT calculations of the thermal conductivities and electrical resistivities of two solid iron alloys, $Fe_{0.96}Si_{0.04}$ and $Fe_{0.85}Si_{0.15}$, to replicate experimental determinations made at the same pressure, temperature and alloy concentrations. We see the onset of resistivity saturation for the 4% mixture, whereas the 15% mixture has already reached its saturated value at the lowest temperature investigated and the resistivity is almost independent of temperature. We compare our thermal conductivity values with direct measurements available in literature. Our DFT calculations do not include EES contributions, which as shown recently could result in an overestimation of the thermal conductivity of up to $\simeq$ 24% (Pourovskii et al., 2020).

Once both computational and experimental uncertainties are taken into account, we find agreement in κ values for both mixtures for at least some of the data. In particular, for the 4% Si mixture, our corrected κ value of 64 W m^{-1} K^{-1} at 72 GPa and 2050 K agrees with the experimental value of 50 ± 15 W m^{-1} K^{-1} measured by Hsieh et al. (2020) at 70 GPa and 2050 K. For the 15% Si mixture, we find a corrected κ value of 66 W m^{-1} K^{-1} at 106 GPa and 3000 K, which is in very good agreement with the value of 60 ± 17 W m^{-1} K^{-1} measured by Hsieh et al. (2020) at the same PT conditions. The comparisons presented in the present work should lend confidence to previously calculated thermal conductivity values at Earth's core conditions, albeit augmented with a larger error estimate due to possible EES processes. Considering

this $\simeq$ 24% reduction in thermal conductivity, our new thermal history models predict a young inner core (400-700 Myrs old) which is still very hot at ancient times, suggesting a basal magma ocean interaction for most of Earth's history.

CRediT authorship contribution statement

MP performed the calculations and produced figures. MP, CD and DA wrote the paper.

Declaration of competing interest

The authors declare that they have no competing interests.

References

Alfè, D., 1999. Ab initio molecular dynamics, a simple algorithm for charge extrapolation. Comput. Phys. Commun. 118, 31–33.

Alfè, D., Pozzo, M., Desjarlais, M.P., 2012. Lattice electrical resistivity of magnetic bcc iron from first-principles calculations. Phys. Rev. B 85, 024102.

Andersen, H.C., 1980. Molecular dynamics simulations at constant pressure and/or temperature. J. Chem. Phys. 72, 2384–2393.

Badro, J., Siebert, J., Nimmo, F., 2016. An early geodynamo driven by exsolution of mantle components from Earth's core. Nature 536, 326–328.

Baum, B.A., Gel'd, P.V., Tyagunov, G.V., 1967. Resistivity of ferrosilicon alloys in the temperature range 800-1700 °C. Phys. Met. Metallogr. 24, 181–184.

Berrada, M., Secco, R.A., 2021. Review of electrical resistivity measurements and calculations of Fe and Fe-alloys relating to planetary cores. Front. Earth Sci. 9, 732289.

Berrada, Secco R.A., Yong, W., Littleton, J.A.H., 2020. Electrical resistivity measurements of Fe-Si with implications for the early lunar dynamo. J. Geophys. Res., Planets 125, e2020JE006380.

Biggin, A., Piispa, E., Pesonen, L., Holme, R., Paterson, G., Veikkolainen, T., Tauxe, L., 2015. Palaeomagnetic field intensity variations suggest Mesoproterozoic inner-core nucleation. Nature 526, 245–248.

Blöchl, P.E., 1994. Projector augmented-wave method. Phys. Rev. B 50, 17953–17979.

Bono, R.K., Tarduno, J.A., Nimmo, F., Cottrell, R.D., 2019. Young inner core inferred from Ediacaran ultra-low geomagnetic field intensity. Nat. Geosci. 12 (2), 143–147.

Bouffard, M., Landeau, M., Goument, A., 2020. Convective erosion of a primordial stratification atop Earth's core. Geophys. Res. Lett. 47 (14), e2020GL087109.

Buffett, B.A., 2012. Geomagnetism under scrutiny. Nature 485, 319–320.

Buffett, B.A., Seagle, C.T., 2010. Stratification of the top of the core due to chemical interactions with the mantle. J. Geophys. Res., Solid Earth 115, B04407.

Chester, G.V., Thellung, A., 1961. The law of Wiedemann and Franz. Proc. Phys. Soc. Lond. 77, 1005–1013.

Davies, C., 2015. Cooling history of Earth's core with high thermal conductivity. Phys. Earth Planet. Inter. 247, 65–79.

Davies, C., Greenwood, S., in press. Dynamics in Earth's core arising from thermo-chemical interactions with the mantle. In: AGU Monograph "Core-Mantle Evolution - a Multidisciplinary Approach". https://doi.org/10.31223/X5MW4G.

Davies, C., Pozzo, M., Gubbins, D., Alfè, D., 2015. Constraints from material properties on the dynamics and evolution of Earth's core. Nat. Geosci. 8, 678–685.

Davies, C., Pozzo, M., Gubbins, D., Alfè, D., 2020. Transfer of oxygen to Earth's core from a long-lived magma ocean. Earth Planet. Sci. Lett. 538, 116208.

Davies, C., Bono, R.K., Meduri, D.G., Aubert, J., Greenwood, S., Biggin, A.J., 2022. Dynamo constraints on the long-term evolution of Earth's magnetic field strength. Geophys. J. Int. 228, 316–336.

de Koker, N., Steinle-Neumann, G., Vlček, V., 2012. Electrical resistivity and thermal conductivity of liquid Fe alloys at high P and T, and heat flux in Earth's core. Proc. Natl. Acad. Sci. 109, 4070–4073.

Desjarlais, M.P., Kress, J.D., Collins, L.A., 2002. Electrical conductivity for warm, dense aluminum plasmas and liquids. Phys. Rev. E 66, 025401(R).

Driscoll, P., Bercovici, D., 2014. On the thermal and magnetic histories of Earth and Venus: influences of melting, radioactivity, and conductivity. Phys. Earth Planet. Inter. 236, 36–51.

Frost, Daniel A., Avery, Margaret S., Buffett, Bruce A., Chidester, Bethany A., Deng, Jie, Dorfman, Susannah M., Li, Zhi, Liu, Lijun, Lv, Mingda, Martin, Joshua F., 2022. Multidisciplinary constraints on the thermal-chemical boundary between Earth's core and mantle. Geochem. Geophys. Geosyst. https://doi.org/10.1029/2021GC009764.

Gomi, H., Ohta, K., Hirose, K., Labrosse, S., Caracas, R., Verstraete, M.J., Hernlund, J.W., 2013. The high conductivity of iron and thermal evolution of the Earth's core. Phys. Earth Planet. Inter. 224, 88–103.

Gomi, H., Hirose, K., Akai, H., Fei, Y., 2016. Electrical resistivity of substitutionally disordered hcp FeSi and FeNi alloys: chemically-induced resistivity saturation in the Earth's core. Earth Planet. Sci. Lett. 451, 51–61.

Greenwood, D.A., 1958. The Boltzmann equation in the theory of electrical conduction in metals. Proc. Phys. Soc. 71, 585–596.

Gubbins, D., Alfè, D., Masters, G., Price, G.D., Gillan, M.J., 2003. Can the Earth's dynamo run on heat alone? Geophys. J. Int. 155, 609–622.

Hausoel, A., Karolak, M., Şaşıoğlu, E., Lichtenstein, A., Held, K., Katanin, A., Toschi, A., Sangiovanni, G., 2017. Local magnetic moments in iron and nickel at ambient and Earth's core conditions. Nat. Commun. 8, 16062.

Helffrich, G., Kaneshima, S., 2010. Outer-core compositional stratification from observed core wave speed profiles. Nature 468, 807–810.

Hirose, K., Morard, G., Sinmyo, R., Umemoto, K., Hernlund, J., Helffrich, G., Labrosse, S., 2017. Crystallization of silicon dioxide and compositional evolution of the Earth's core. Nature 543, 99–102.

Hsieh, W.-P., Goncharov, A.F., Labrosse, S., Holtgrewe, N., Lobanov, S.S., Chuvashova, I., Deschamps, F., Lin, J.-F., 2020. Low thermal conductivity of iron-silicon alloys at Earth's core conditions with implications for the geodynamo. Nat. Commun. 11 (1), 1–7.

Inoue, H., Suehiro, S., Ohta, K., Hirose, K., Ohishi, Y., 2020. Resistivity saturation of hcp Fe-Si alloys in an internally heated diamond anvil cell: a key to assessing the Earth's core conductivity. Earth Planet. Sci. Lett. 543, 116357.

Ioffe, A.F., Regel, A.R., 1960. Non-crystalline, amorphous and liquid electronic semiconductors. Prog. Semicond. 4, 237–291.

Konôpková, Z., McWilliams, R., Gómez-Pérez, N., Goncharov, A., 2016. Direct measurement of thermal conductivity in solid iron at planetary core conditions. Nature 534, 99–101.

Kresse, G., Furthmuller, J., 1996. Efficiency of ab-initio total energy calculations for metals and semiconductors using a plane-wave basis set. Comput. Mater. Sci. 6, 15–50.

Kresse, G., Joubert, D., 1999. From ultrasoft pseudopotentials to the projector augmented-wave method. Phys. Rev. B 59, 1758–1775.

Kubo, R., 1957. Statistical-mechanical theory of irreversible processes. I. General theory and simple applications to magnetic and conduction problems. J. Phys. Soc. Jpn. 12, 570–586.

Labrosse, S., 2015. Thermal evolution of the core with a high thermal conductivity. Phys. Earth Planet. Inter. 247, 36–55.

Labrosse, S., Poirier, J.-P., Le Moeul, J.-L., 2001. The age of the inner core. Earth Planet. Sci. Lett. 190, 111–123.

Landeau, M., Aubert, J., Olson, P., 2017. The signature of inner-core nucleation on the geodynamo. Earth Planet. Sci. Lett. 465, 193–204.

Masters, G., Gubbins, D., 2003. On the resolution of density within the Earth. Phys. Earth Planet. Inter. 140, 159–167.

Mittal, T., Knezek, N., Arveson, S.M., McGuire, C.P., Williams, C.D., Jones, T.D., Li, J., 2020. Precipitation of multiple light elements to power Earth's early dynamo. Earth Planet. Sci. Lett. 532, 116030.

Nimmo, F., 2015. Thermal and compositional evolution of the core. In: Schubert, G. (Ed.), Treatise on Geophysics, vol. 9. Elsevier, Amsterdam, pp. 201–219.

Nimmo, F., Alfè, D., 2007. Properties and evolution of the Earth's core and geodynamo. In: Sammons, P.R., Thompson, J.M.T. (Eds.), Advances in Earth Science: From Earthquakes to Global Warming. In: Royal Society Series on Advances in Science. Imperial College Press, pp. 167–210.

Nosé, S., 1984. A molecular dynamics method for simulations in the canonical ensemble. Mol. Phys. 52, 255–268;
A unified formulation of the constant temperature molecular dynamics methods. J. Chem. Phys. 81, 511–519.

Ohta, K., Kuwayama, Y., Shimizu, K., Yagi, T., Hirose, K., Ohishi, Y., 15–19 December 2014. Measurements of electrical and thermal conductivity of iron under Earth's core conditions. In: AGU Abstract MR21B-06, AGU Fall Meeting. S. Francisco.

Ohta, K., Suehiro, S., Hirose, K., Ohishi, Y., 16–21 August 2015. The electrical resistivity of iron alloys at Earth's core conditions. In: Goldschmidt Conference 2015 Abstract, A2326. Prague, Czech Republic.

Ohta, K., Kuwayama, Y., Hirose, K., Shimizu, K., Ohishi, Y., 2016. Experimental determination of the electrical resistivity of iron at Earth's core conditions. Nature 534, 95–98.

O'Rourke, J.G., Stevenson, D.J., 2016. Powering Earth's dynamo with magnesium precipitation from the core. Nature 529, 387–389.

Pourovskii, L.V., Mravlje, J., Georges, A., Simak, S.I., Abrikosov, I.A., 2017. Electron-electron scattering and thermal conductivity of ϵ iron at Earth's core conditions. New J. Phys. 19, 073022.

Pourovskii, L., Mravlje, J., Pozzo, M., Alfè, D., 2020. Electronic correlations and transport in iron at earth's core conditions. Nat. Commun. 11 (1), 1–8.

Pozzo, M., Alfè, D., 2016a. Saturation of electrical resistivity of solid iron at earth's core conditions. SpringerPlus 5 (1), 1–6.

Pozzo, M., Alfè, D., 2016b. Electrical resistivity saturation of solid iron at Earth's core conditions from density functional theory. In: AGU Abstract DI13A-2356, AGU Fall Meeting. San Fransisco, CA.

Pozzo, M., Desjarlais, M.P., Alfè, D., 2011. Electrical and thermal conductivity of liquid sodium from first-principles calculations. Phys. Rev. B 84, 054203.

Pozzo, M., Davies, C., Gubbins, D., Alfè, D., 2012. Thermal and electrical conductivity of iron at Earth's core conditions. Nature 485, 355–358.

Pozzo, M., Davies, C., Gubbins, D., Alfè, D., 2013. Transport properties for liquid silicon-oxygen-iron mixtures at Earth's core conditions. Phys. Rev. B 87, 014110.

Pozzo, M., Davies, C., Gubbins, D., Alfè, D., 2014. Thermal and electrical conductivity of solid iron and iron-silicon mixtures at Earth's core conditions. Earth Planet. Sci. Lett. 393, 159–164.

Secco, R.A., 2017. Thermal conductivity and Seebeck coefficient of Fe and Fe-Si alloys: implications for variable Lorenz number. Phys. Earth Planet. Inter. 265, 23–34.

Sha, X., Cohen, R.E., 2011. First-principles studies of electrical resistivity of iron under pressure. J. Phys. Condens. Matter 23, 075401.

Silber, R.E., Secco, R.A., Yong, W., Littleton, J.A.H., 2019. Heat flow in Earth's core from invariant electrical resistivity of Fe-Si on the melting boundary to 9 GPa: do light elements matter? J. Geophys. Res., Solid Earth 124, 5521–5543.

Stacey, F.D., Anderson, O.L., 2001. Electrical and thermal conductivities of Fe-Ni-Si alloy under core conditions. Phys. Earth Planet. Inter. 124, 153–162.

Stacey, F.D., Loper, D.E., 2007. A revised estimate of the conductivity of iron alloy at high pressure and implications for the core energy balance. Phys. Earth Planet. Inter. 161, 13–18.

Tarduno, J., et al., 2010. Geodynamo, solar wind, and magnetopause 3.4 to 3.45 billion years ago. Science 327, 1238–1240.

Wang, Y., Perdew, J.P., 1991. Correlation hole of the spin-polarized electron gas, with exact small-wave-vector and high-density scaling. Phys. Rev. B 44, 13298–13307;
Perdew, J.P., Chevary, J.A., Vosko, S.H., Jackson, K.A., Pederson, M.R., Singh, D.J., Fiolhais, C. Atoms, molecules, solids, and surfaces: applications of the generalized gradient approximation for exchange and correlation. Phys. Rev. B 46, 6671–6687 (1992).

Xiong, Z., Tsuchiya, T., Taniuchi, T., 2018. Ab initio prediction of potassium partitioning into Earth's core. J. Geophys. Res., Solid Earth 123, 6451–6458.

Xu, J., Zhang, P., Haule, K., Minar, J., Wimmer, S., Ebert, H., Cohen, R., 2018. Thermal conductivity and electrical resistivity of solid iron at Earth's core conditions from first principles. Phys. Rev. Lett. 121 (9), 096601.

Zhang, Y., Hou, M., Liu, G., Zhang, C., Prakapenka, V.B., Greenberg, E., Fei, Y., Cohen, R., Lin, J.-F., 2020. Reconciliation of experiments and theory on transport properties of iron and the geodynamo. Phys. Rev. Lett. 125 (7), 078501.